Journal of the Korean Physical Society (2023) 82:32–39
https://doi.org/10.1007/s40042-022-00686-6

Online ISSN 1976-8524
Print ISSN 0374-4884

ORIGINAL PAPER - FLUIDS, PLASMA AND PHENOMENOLOGY

General parametric dependence of atmospheric pressure argon plasmas

Seokyong Jeong[1] · Jimo Lee[2] · Gunsu Yun[1,3]

Received: 8 November 2022 / Revised: 25 November 2022 / Accepted: 25 November 2022 / Published online: 13 December 2022

Abstract
Using a global model for atmospheric pressure plasma, we investigated general dependence of plasma properties on power density and plasma size. We built a global simulation for a pure argon cylindrical plasma and observed changes in plasma properties with the power density and plasma size. The study of the power dependence shows that the density of excited species is in general proportional to the power when the power density is low, whereas the density becomes saturated when the power density becomes high enough. These trends are explained by a generalized form of particle balance equation, implying that the same trends for reactive species density would emerge in various plasma conditions. For the plasma size dependence, the electron density increases and the electron temperature decreases for increasing plasma size. Both become saturated when the plasma size becomes large enough. These trends of electron density and temperature are explained by the relative change of the diffusive loss. Our simulation results give a useful insight into the tendency of plasma properties over a wide range of plasma parameters.

Keywords Cold plasma · Plasma modeling · Plasma simulation · Atmospheric pressure plasma

1 Introduction

Cold plasma can generate beneficial chemical properties that general heating methods cannot obtain. In particular, atmospheric pressure plasma has received much attention because it can be treated to biological tissue without thermal damage. Various studies have investigated the effect of plasma on living tissue and the possibility of its application in agriculture and medicine [1–14]. Several studies have proven the effectiveness of plasma in the treatment of various skin diseases [6–8], wound healing [9–12], and scar removal [13]. Plasma skincare devices that help the absorption of active ingredients have been commercialized [14].

Another notable application of cold plasma is a material fabrication. Cold plasma can change the properties of a material by the collision of the energetic electron while maintaining the structure of the material due to low gas temperature [15]. Plasma surface treatment on carbon-based materials such as graphene and carbon nanotubes can make the surface hydrophilic while maintaining the structure [16–19]. Plasma treatment can also tune oxygen vacancies on the metal oxide surface [20–25].

In most of the applications mentioned above, reactive oxygen–nitrogen species (RONS) generated in plasma play an essential role. RONSs are generated by the collision of energetic electrons with air molecules. The collision rate depends on the plasma properties such as electron temperature, electron density, etc. We can control the plasma properties by changing operating conditions.

This study aims to provide guidelines for controlling plasma properties by examining the parametric dependency of plasma properties on operating conditions. We performed global simulations in various operating conditions and observed the dependency of the electron temperature, electron density, and excited species density. We analyzed the simulation results and revealed the mechanism of parametric

✉ Gunsu Yun
gunsu@postech.ac.kr

[1] Department of Physics, Pohang University of Science and Technology, Pohang 37673, Republic of Korea

[2] Mechatronics Research, Samsung Electronics Co., Ltd, Hwaseong-si, Republic of Korea

[3] Division of Advanced Nuclear Engineering, Pohang University of Science and Technology, Pohang 37673, Republic of Korea

dependency, which will enhance the understanding of cold plasma.

Plasma properties greatly depend on plasma driving conditions. The gas composition determines the ionization efficiency and the chemical products, including radicals. The noble gas is used as the loading gas to increase the ionization efficiency. Noble gases usually exist as single atomic molecules, and the transmitted power is not converted into vibrational or rotational energy. Depending on the target chemical species, a gas such as air or a fluorocarbon compound would be mixed. The heating mechanism of the plasma may vary according to the frequency of the power source, such as DC, RF, or microwave.

This research focuses on the parametric dependency of plasma properties according to the electric power change and plasma size. Changing the power has a significant effect on plasma chemistry without changing the shape of the electrode. An increase in power can be expected to improve the production of reactive species, but power efficiency may not be constant. One of the objectives of this study is to investigate the trend of power efficiency. The shape and size of the electrodes are greatly limited to optimize the power transfer efficiency. Accordingly, it is not easy to independently change the size of the plasma. However, the size of the plasma is a parameter that determines the effect of diffusion and greatly influences the plasma's chemical properties. We will independently change the plasma size under the numerical simulation and analyze the effect of plasma size.

The global model does not calculate the plasma's spatial distribution but sets the plasma's physical properties (electron temperature, the density of each species, sheath thickness, power, etc.) as a single scalar value representing the entire plasma and focuses on calculating the time dependence. Various global models simulate plasma, but in this study, a model similar to the collisional radiative model (CR model) was used, which calculates the reaction rate and the density of the plasma bulk to predict the radiation spectrum of the plasma. Since the goal of this research is not to predict the complete radiation spectrum but to determine the plasma properties' tendency, relatively simplified excitation levels were used.

The first advantage of the global model is its low computational load. Since the global model ignores the spatial distribution, the computational load is not significantly increased when the chemical species and corresponding reactions are added. Because of this, hundreds of reaction equations and dozens of chemical species can be handled simultaneously. On the one hand, we can compare the results of various operating conditions due to the short simulation time.

The second advantage of the global model is its high stability. A spatial-dependent model should set the appropriate spatial grid according to the simulation geometry or operating conditions. The simulation will not converge to a steady state if the grid is too sparse or even too dense. On the other hand, the global simulation does not require the spatial grid, so we can easily change the operating conditions to maintain stability. The global model is advantageous for parametric studies because it can perform simulations more stably under a broader range of operating conditions.

2 Methods

We adopted the global model of COMSOL Multiphysics® for our research. Only the governing equations of the global model are introduced here. For more details, please refer to the COMSOL Multiphysics manual [26]. The global model mainly consists of particle balance and power balance equations. The particle balance equation calculates the density of each species, and the power balance equation determines the electron temperature. Equation (1) shows the simplified particle balance equation omitting the terms ignored in the current simulation condition.

$$V\rho\frac{dw_s}{dt} = V\sum_{j\in\text{react.}} m_s\Delta_{js}r_j + Am_sR_{s,} \tag{1}$$

where V is the system volume, ρ is the mass density of the gas mixture, w_s is the mass fraction of species s, and m_s is the particle mass of species s. The first term on the right-hand side corresponds to the summation of the generation and consumption rate of species s by all reactions, where r_j is the rate of the j th reaction per unit volume and Δ_{js} is the number of particles produced or reduced by the reaction j. The second term corresponds to the boundary loss or source of species s, where R_s is the total boundary particle flux of species s (with the sign convention of negative R_s for net loss), A is the surface area of the plasma. The boundary particle flux R_k is given by

$$R_s = -n_s v_{s,\text{eff}}, \tag{2}$$

where n_s is the number density of species s and $v_{s,\text{eff}}$ is the effective diffusion speed [27]. $v_{s,\text{eff}}$ is the harmonic mean of diffusive speed and thermal speed for neutral species. In the case of ions, $v_{s,\text{eff}}$ is given by $h \cdot v_B$, where v_B is Bohm velocity, and h is the ratio of the electron density in sheath to the density in bulk. Note that $h \cdot v_B$ approachs to the harmonic mean of Bohm velocity and ambipolar diffusion speed at a high-pressure limit [28]. Our model can be expanded to low-pressure or intermediate-pressure conditions with an appropriate value of h, provided by Sect. 10.2 of Lieberman textbook [28]. More details about the effective diffusion speed are explained in our previous study [27].

Since this global model focuses on the bulk properties of plasma, the quasi-neutrality condition should be satisfied.

The quasi-neutrality condition determines the electron density n_e as followed:

$$0 = \sum_{s\in \text{sp.}} q_s n_s - e n_e, \tag{3}$$

where q_s is the electric charge of species s, and $-e$ is the electron charge.

Most of the plasmas used under atmospheric pressure application are non-thermal plasmas, in which the electron temperature and the gas temperature are different in general. Since the electron temperature is an important parameter that determines the reaction coefficients of electron collision reactions, building a consistent model for electron temperature is necessary. The electron temperature is defined by electron energy density n_ϵ and electron density n_e as follows: $T_\text{e} = \frac{2}{3}\frac{n_\epsilon}{n_e}$. We can infer the electron energy density from the power balance equation. Equation (4) is the power balance equation used in this model.

$$\frac{dn_\epsilon}{dt} = P_\text{abs} + \sum_{j\in\text{react.}} E_j r_j + \frac{1}{V}\sum_{i\in+\text{ions}} \left(q_i\left(\Phi_p + \Phi_s\right) + 2T_e\right) A R_i. \tag{4}$$

P_abs, the first term of RHS, is power density absorbed to plasma bulk. The second term corresponds to total electron energy dissipation by reactions, where E_j is energy generation or loss per occurrence of reaction j. The third term is total energy loss by electron and ion diffusion, where V is the simulation volume and A is the boundary surface area. Φ_p and Φ_s are plasma potential and sheath potential, respectively. When an ion escapes the plasma bulk by diffusion, the plasma potential and sheath potential accelerate the ion by $q_i\left(\Phi_p + \Phi_s\right)$ and this amount of energy is consumed from the plasma. Because our model supposes the quasi-neutrality, the same number of electrons diffuses out as ions. The diffused electron has a kinetic energy of $2T_e$[28]. For the low voltage sheath and high-pressure condition ($\lambda_i \le LT_i/T_e$, where λ_i is the ion mean free path, and L is the system size), the plasma and sheath potentials are approximated as follows [27, 29] (note that the electron temperature is expressed in the unit of voltage):

$$V_p \cong \frac{1}{2}T_e, \tag{5}$$

$$V_s \cong \ln\left(4\frac{\overline{u_B}}{v_e}\right)T_e. \tag{6}$$

We constructed the reaction set assuming pure argon plasma. Seven species were considered for the model: Ar, Ar(4s), Ar(4p), Ar^+, $Ar_2^+$$Ar_2^*$, and electron. Ar(4 s) represents a population of four excited argon levels with an energy of 11.54–11.72 eV. Ar(4p) represents a population of ten excited argon levels with an energy of 12.9–13.5 eV. Ar^+ and Ar_2^+ represent monoatomic ions and diatomic ions, respectively. Ar_2^* is an excimer of argon, which is the lowest energy level among the stable excited levels of argon dimers. Table 1 shows all reactions and reaction constants used in this simulation.

For reactions 1–17, the model calculates reaction rate coefficient (k_r) using cross section data ($\sigma(\epsilon)$) as follows:

$$k_r = \sqrt{\frac{2q}{m_e}}\int \epsilon\sigma(\epsilon) f_\text{eepf}(\epsilon) d\epsilon, \tag{7}$$

where ϵ is electron energy, $\sigma(\epsilon)$ is cross section, and $f_\text{eepf}(E)$ is electron energy probability function (EEPF). In many plasma models, the EEPF is assumed to be follows a Maxwell distribution or a Druyvesteyn distribution to calculate the reaction rate. However, EEPF has a complex dependency on the electron density, the type of electron collision reaction, and the population of field particles. Our model used the two-term Boltzmann equation solver embedded in the COMSOL Multiphysics® plasma simulator to calculate the EEPF [26]. This solver updates the EEPF in each time step depending on the electron density, electron temperature, densities of the individual species interacting with electrons, and their cross sections. In general, the Boltzmann solver can calculate T_e from given E/N, but this model is designed to find E/N that gives the same T_e as T_e calculated from the power balance equation.

Parameters other than power density and plasma size were fixed. The gas temperature of pure argon at atmosphere pressure was assumed to be 800 K. This condition is same as the experimental condition in the previous study, atmospheric pressure microwave plasma [42]. The geometry of plasma volume is cylindrical. For the case of power sweeping (from 0.001 W to 10,000 W), the radius and height were set to 2 mm and 4 mm, respectively. For the case of volume sweeping, the power density was fixed to 100 W/cm^3, while radius changes from 0.02 mm to 200 mm, maintaining the aspect ratio of cylinder. The global simulation calculates the plasma state after driving for one second, which is sufficient to reach equilibrium.

3 Results

The dominant ion species changes to atomic ion from dimer ion with increasing power. Below about 80 W, the population ratio Ar_2^+ to Ar^+ is almost constant because the population is determined by the balance between the attachment (24 in Table 1) and diffusion. However, as the power density increases, the dissociative recombination of Ar_2^+ (reaction 14) reduces Ar_2^+ population (see Fig. 1a). Figure 2d) shows that the dominant source of Ar_2^+ is the attachment of Ar^+

Table 1 Reactions included in the global simulation for pure Ar plasma

#	Equation	A	n	E_a	Energy	Ref
r1	$e + Ar \Rightarrow e + Ar$	σ(ϵ)			*	[30]
r2	$e + Ar \Rightarrow e + Ar(4s)$	σ(ϵ)			11.6	[30]
r3	$e + Ar(4s) \Rightarrow e + Ar$	σ(ϵ)			− 11.6	[a]
r4	$e + Ar \Rightarrow e + Ar(4p)$	σ(ϵ)			13.2	[30]
r5	$e + Ar(4p) \Rightarrow e + Ar$	σ(ϵ)			− 13.2	[a]
r6	$e + Ar(4s) \Rightarrow e + Ar(4p)$	σ(ϵ)			1.6	[b]
r7	$e + Ar(4p) \Rightarrow e + Ar(4s)$	σ(ϵ)			− 1.6	[a]
r8	$e + Ar \Rightarrow 2e + Ar^+$	σ(ϵ)			15.76	[30]
r9	$e + Ar(4s) \Rightarrow 2e + Ar^+$	σ(ϵ)			4.16	[30]
r10	$e + Ar(4p) \Rightarrow 2e + Ar^+$	σ(ϵ)			2.76	[30]
r11	$e + Ar_2^* \Rightarrow 2e + Ar_2^+$	σ(ϵ)			3.8	[c]
r12	$2e + Ar^+ \Rightarrow e + Ar$	σ(ϵ)			− 15.76	[d]
r13	$2e + Ar^+ \Rightarrow e + Ar(4s)$	σ(ϵ)			− 4.16	[d]
r14	$2e + Ar^+ \Rightarrow e + Ar(4p)$	σ(ϵ)			− 2.76	[d]
r15	$e + Ar^+ \Rightarrow Ar$	σ(ϵ)				[e]
r16	$e + Ar^+ \Rightarrow Ar(4s)$	σ(ϵ)				[e]
r17	$e + Ar^+ \Rightarrow Ar(4p)$	σ(ϵ)				[e]
r18	$e + Ar_2^+ \Rightarrow Ar + Ar(4s)$	6.86E− 08	− 0.61			[f],[31]
r19	$e + Ar_2^+ \Rightarrow Ar + Ar(4p)$	2.94E− 08	− 0.61			[f],[31]
r20	$e + Ar_2^+ \Rightarrow e + Ar + Ar^+$	1.36E− 06		2.094	1.5	[32, 32]
r21	$e + Ar_2^* \Rightarrow e + Ar + Ar$	1.00E− 09			− 10.5	[32, 32]
r22	$Ar_2^* + Ar_2^* \Rightarrow e + 2Ar + Ar_2^+$	1.00E− 09				[34]
r23	$Ar_2^* \Rightarrow 2Ar$	6.00E+07				[32, 32]
r24	$2Ar + Ar^+ \Rightarrow Ar + Ar_2^+$	2.50E− 31				[32, 32]
r25	$2Ar + Ar(4s) \Rightarrow Ar + Ar_2^*$	2.50E− 32				[32, 32]
r26	$2Ar + Ar(4p) \Rightarrow Ar + Ar_2^*$	3.30E− 31				[32, 32]
r27	$Ar + Ar(4p) \Rightarrow Ar + Ar(4s)$	3.00E− 12				[32, 32]
r28	$Ar + Ar(4s) \Rightarrow Ar + Ar$	2.00E− 15				[32, 32]
r29	$Ar(4s) + Ar_2^* \Rightarrow e + Ar + Ar_2^+$	6.00E− 10	0.5			[32, 32]
r30	$Ar(4s) + Ar(4p) \Rightarrow e + Ar + Ar^+$	5.00E− 10	0.5			[38]
r31	$Ar(4s) + Ar(4s) \Rightarrow e + Ar + Ar^+$	5.00E− 10	0.5			[38]
r32	$Ar(4p) + Ar(4p) \Rightarrow e + Ar + Ar^+$	7.00E− 10	0.5			[38]
r33	$Ar(4s) + Ar(4s) \Rightarrow e + Ar_2^+$	6.30E− 10	− 0.5			[32, 32]
r34	$Ar(4p) \Rightarrow Ar(4s)$	3.76E+08				[40]

For reactions 1–17, indicated by $\sigma(\epsilon)$, the reaction rate is determined using the two-term Boltzmann equation solver and cross-section data. The rates coefficient of reactions 62–91 are given in the Arrhenius form: $k = A \cdot (T)^n exp\left(-\frac{E_a}{T}\right)$. The unit of A is s^{-1}, cm^3s^{-1}, and cm^6s^{-1} for the first-, second-, and third-order reactions, respectively. The unit of temperature T is K for heavy particle reactions and eV for electron collision reactions. The unit of E_a is the same as that of T.

*The electron energy loss by elastic collision is given by $m_r \cdot 3(T_g - T_e)$, where m_r is mass fraction of electron and argon.

[a]The cross section is calculated under the principle of detailed balance using corresponding excitation cross-section data [41].

[b]Empirical cross section of electron impact excitation taken from [40], 40

[c]Empirical cross section of electron impact ionization taken from [40], 40

[d]The cross section is calculated under the principle of detailed balance, considering it as the inverse reaction of electron impact ionization [41].

[e]The cross section is calculated under the principle of detailed balance, considering it as the inverse reaction of photo-ionization. The cross section of photo-ionization is taken from [36].

[f]The dissociative recombination coefficients are calculated based on the known reaction coefficient

(reaction 24) for the whole range, and the dominant loss is the diffusive loss for low power and the dissociative recombination (reaction 14) for high power. In equilibrium, the total consumption and production must balance each other. The equilibrium between the production and consumption of Ar_2^+ is established as follows:

$$\left[Ar_2^+\right][e^-]k_{\mathrm{rec(g)}} + \left[Ar_2^+\right]k_{\mathrm{diff}(Ar_2^+)} \approx \left[Ar^+\right][Ar]^2 k_{\mathrm{att}+}, \quad (8)$$

where $k_{\mathrm{att}+}$ and $k_{\mathrm{rec(g)}}$ represent the rate coefficient of attachment of Ar^+ and recombination reaction generating argon ground state, respectively. The effective diffusion rate coefficient k_{diff} is given by $k_{\mathrm{diff}(Ar_2^+)} = v_{B,Ar_2^+}/(V/S)$. These three rate coefficients are approximately constant for the simulation power range. One can rearrange Eq. (10) as follows to obtain the ion ratio α:

$$\alpha \equiv \frac{\left[Ar_2^+\right]}{\left[Ar^+\right]} \approx \frac{[Ar]k_{\mathrm{att}}}{[e^-]k_{\mathrm{rec(g)}} + k_{\mathrm{diff}(Ar_2^+)}}. \quad (9)$$

In the condition of $[e^-]k_{\mathrm{rec(g)}} \ll k_{\mathrm{diff}(Ar_2^+)}$ (below 10 W for our simulation), the ion ratio α is approximately constant. For $P_{\mathrm{abs}} \cdot V = P_{\mathrm{tot}} > 10$W, where the loss by diffusion and recombination become comparable, α is no longer constant but decreases with increasing n_e. Note that the ion ratio α is over unity for low-power conditions due to the high ground argon density. As a contrasting comparison, α would be smaller than unity for low-pressure argon discharges, where the dominant ion species would be the monatomic argon ions.

The ionization efficiency n_e/P_{abs} increases with P_{tot} because the dominant ionization reaction changes from the impact ionization from the ground state (reaction 8) to the impact ionization from Ar(s) (reaction 9) as n_e

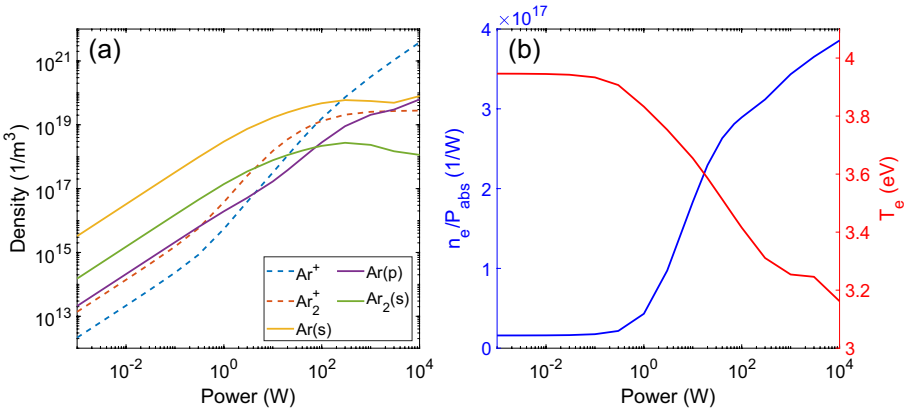

Fig. 1 Results of the CW simulations for different power densities. a Equilibrium density of each species and b equilibrium electron temperature and electron density normalized by the power density

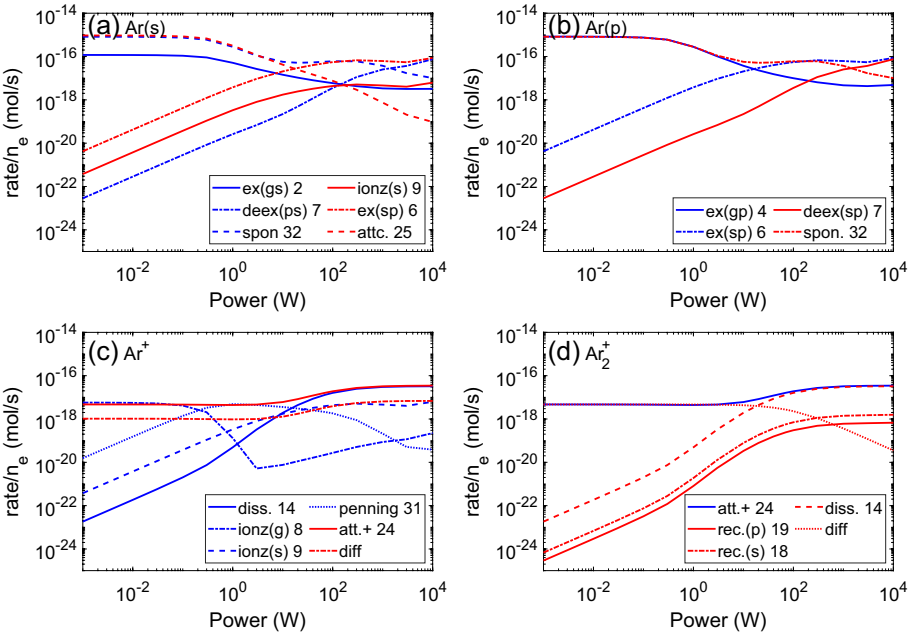

Fig. 2 Power dependence of the equilibrium reaction rate normalized by the electron density. Here, r in the y-axis represents the reaction rate of each reaction. The numbers in the legends are the corresponding reaction numbers in Table 1

increases. Since the recombination loss of Ar^+ is negligible ($[e^-]k_{rec} \ll k_{diff}$), the balance equation of Ar^+ is as follows:

$$\left[Ar^+\right][Ar]^2 k_{att+} + \left[Ar^+\right]k_{diff(Ar^+)} \approx [Ar][e^-]k_{ionz(g)} + [Ar(s)][e^-]k_{ionz(s),} \tag{10}$$

$$\frac{1}{(1+\alpha)}\left([Ar]^2 k_{att+} + k_{diff(Ar^+)}\right) \approx [Ar]k_{ionz(g)} + [Ar(s)]k_{ionz(s),} \tag{11}$$

where $k_{ionz(g)}$ and $k_{ionz(s)}$ represent the rate coefficient of the ionization from Ar and Ar(s), respectively, and the charge neutrality condition is used, $[e^-] = \left[Ar_2^+\right] + \left[Ar^+\right] = (1+\alpha)\left[Ar^+\right]$. Hereinafter, we express the rate coefficient of ionization from state 'a' as $k_{ionz(a)}$. Further, $k_{ionz(s)}$ is approximately constant in our simulation range, while $k_{ionz(g)}$ is more sensitive to T_e because it consumes higher electron energy (~ 15.8 eV). It should be noted that the left side of Eq. (15) is almost constant. In high-power conditions, the ionization of Ar(s) becomes the dominant ionization process due to the high density of Ar(s). Therefore, $k_{ionz(g)}$ decreases to maintain the right-hand side of Eq. (15), which means T_e decreases. From a different perspective, as the population of Ar(s) increases, ionization occurs more efficiently at lower electron temperatures and thus, n_e/P_{abs} increases with P_{tot}(see Fig. 1b).

In the low-power region ($P < 10^{-2}$W), the density of all the reaction species increases almost linearly with the power. However, the species (except Ar^+) are saturated at specific high power. Figure 2a shows that the dominant production and consumption reactions of Ar(s) vary according to P_{tot}. The excitation (reaction 2) and quenching (reaction 28) are the dominant generation and consumption reactions in the low-power region. The balance equation at this condition is then as follows:

$$[Ar]^2[Ar(s)]k_{r26} \approx \left[Ar(p)\right]k_{spon}, \tag{12}$$

where k_{r26} and k_{spon} are the reaction coefficient of reaction 26 of Table 1 and the spontaneous emission rate coefficient from Ar(p) to Ar(s), respectively. In the low-power range, both [Ar(p)] and [Ar(s)] are proportional to n_e, and therefore, $[Ar(s)] \propto [Ar(p)]$.

Conversely, in the high-power range, Ar(s) excitation to Ar(p) becomes the dominant consumption reaction. The balanced equation for Ar(s) at high power is as follows:

$$[e^-][Ar(s)]k_{ex(sp)} \approx \left[Ar(p)\right]k_{spon} + [e^-]\left[Ar(p)\right]k_{ex(ps)} \propto [Ar(p)], \tag{13}$$

where $k_{ex(sp)}$ and $k_{ex(ps)}$ are reaction coefficient of electron impact excitation from Ar(s) to Ar(p) and reverse reaction(de-excitation). Hereinafter, we express the rate coefficient of excitation and de-excitation from 'a' to 'b' as $k_{ex(ab)}$. In Eq. (17), the RHS is the same as the sum of the dominant consumption reactions of Ar(p), which is proportional to [Ar(p)]. This implies that the density of Ar(s) is proportional to the density of Ar(p) divided by electron density. Since [Ar(p)] increases proportionally to $[e^-]$ in the high-power region, [Ar(s)] will remain approximately constant.

The density trend (increase with power and then saturate) is generally observed in reactive species. We suggest the generalized balance equation to explain this tendency as follows:

$$\left[M^*\right] \cdot C_1 + \left[M^*\right] \cdot n_e \cdot C_2 = n_e \cdot C_3, \tag{14}$$

where $[M^*]$ is the density of an excited species and C_n represents other dependences like the reaction coefficient or the reactant density. LHS of the equation represents the dominant losses of species $[M^*]$ and RHS represents the dominant generations. The generation rate should be proportional to n_e because the electron collision reaction must be involved due to its high energy level. Even if the electron impact reaction does not directly generate the species $[M^*]$ like Penning ionization, the reactants of the dominant reactions should be generated by electron collision reactions. The loss reactions on the LHS are obviously proportional to $[M^*]$ itself because $[M^*]$ is the reactant. To explain the dependence on n_e, we assume two cases for loss channel, one with and the other without n_e dependence. For example, the quenching or spontaneous reaction does not have n_e dependence, while electron collision reaction like de-excitation is proportional to n_e. For low n_e, the loss channel with n_e dependence (second term in Eq. (20)) is negligible, i.e., $[M^*] \cdot C_1 \approx n_e \cdot C_3$. If the C_n are independent on n_e(generally true), $[M^*] \propto n_e$. For high n_e where $[M^*] \cdot C_1 \ll [M^*] \cdot n_e \cdot C_2$, the first term of Eq. (20) becomes negligible and $[M^*] \cdot n_e \cdot C_2 \approx n_e \cdot C_3$, implying that $[M^*]$ is almost constant. Similar trends in densities of the Ar excited states are observed in the spectroscopic study of atmospheric pressure argon plasma torch experiments by Rincon et al. (2013) [42]. The study showed that the intensities of Ar I line emission increase with power and become saturated at high power, which is consistent with our model prediction.

We studied the dependence of the equilibrium density on the plasma volume under fixed power density. The ion species tend to increase with length scale, while the neutral species decrease after slight increase. Note that the increase of ion density is equivalent to the increase of electron density. The electron density is approximately proportional to (V/A) for low (V/A). Figure 3 shows the equilibrium density variations of each species with varying plasma volume (the aspect ratio of the cylinder is maintained). Referring to Eq. (3), the diffusion rate per volume $r_{diff} = \frac{n_k v_{k,eff}}{(V/A)}$. In small (V/A) conditions, volumetric energy loss channels like the

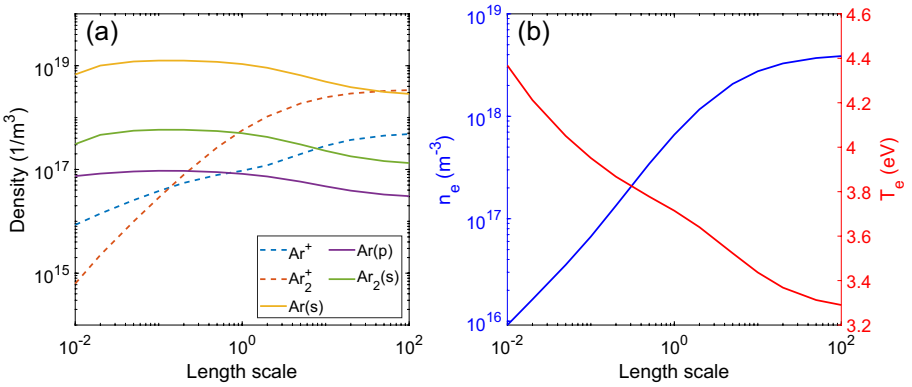

Fig. 3 Result of the CW simulation with varying plasma volume. Length scale means the length ratio with respect to the original size (a cylinder with a length of 4 mm and radius of 2 mm). **a** Equilibrium density of each species and **b** equilibrium electron temperature and electron density

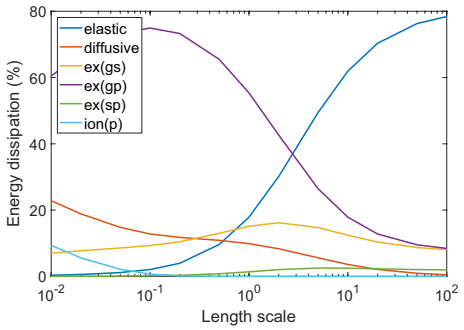

Fig. 4 Length scale dependence of the electron energy dissipation portion

elastic collision, spontaneous emission, quenching of excited species are negligible (see Fig. 4). Therefore, the only energy loss channel is diffusive loss and the summation of reactional energy loss in the power balance equation (the second term of Eq. 5) is approximately the same with ionization energy of escaping ions, i.e., $\sum_{j\in\text{react.}} E_j r_j \approx \sum_{\text{k}\in\text{ions}} W_\text{k} r_{\text{diff,k}}$, where W_k is the ionization energy of ion k. The power balance Eq. (5) can be rewritten as follows:

$$P_\text{abs} \approx \sum_{i\in+\text{ions}} \left(W_i + \left(q_i\left(\Phi_p + \Phi_s\right) + 2T_e\right)\right)\frac{n_i v_{i,\text{eff}}}{(V/A)}. \qquad (15)$$

In our simulation, while the length scale changed from 0.01 to 1, the term $\left(W_i + \left(q_i\left(\Phi_p + \Phi_s\right) + 2T_e\right)\right)v_{\text{k,eff}}$ decreased only by 30 percent. Thus, when the power density P_abs is maintained, $\sum_{i\in+\text{ions}} n_k = n_e$ is approximately proportional to (V/A). As (V/A) increases, the total diffusive energy loss decreases, and the elastic collisional energy loss becomes the dominant energy loss channel. When the diffusive loss is negligible, the elastic energy loss should be balanced with P_abs. Therefore, n_e is saturated at $n_e = P_\text{abs}/E_\text{elas}k_\text{elas}[\text{Ar}]$ when (V/A) is sufficiently high. Due to the charge neutrality, ion densities also increase with length scale.

The tendencies of the excited state densities are determined by the competition between two opposite effects: increasing n_e and decreasing T_e. Those two trends of plasma properties act competitively for the generation of excited neutral species: increase of n_e enrich the reactant of the excitation and decrease of T_e reduce the coefficient of the excitation. For very low (V/A), densities of neutral excited species increase with (V/A) because the effect of increasing n_e is more significant. After n_e become saturated, the excited state density decreases with T_e because the reaction coefficients are reduced. If (V/A) is large enough that the effect of diffusive loss is negligible, then the change in (V/A) does not affect the production–consumption balance of each species. That is, the densities will converge to the densities of no diffusion condition.

4 Conclusion

Using global simulation, we have investigated the parametric dependence of plasma properties on power and plasma size. The trend of the results is consistent with our intuition based on particle balance and energy balance equations. The electron temperature and electron density calculated in the model coincided with the values commonly measured experimentally in atmospheric pressure plasma in order of magnitude.

The ionization efficiency (electron density per unit power) increases rapidly as the power increases. A shift in the dominant ionization pathway explains the increase in ionization efficiency. When the power density is high enough, the ionization of the excited argon (step ionization) becomes the dominant ionization. Since the step ionization can efficiently occur at lower electron energies, the energy consumed by ionization increases, and the electron temperature in the equilibrium state decreases.

In a very high-power environment, more power may not guarantee the more production of excited species. The density of several species increases proportionally with increasing power and then becomes saturated. We analyzed this tendency based on the particle balance equation. We presented a generalized balance equation that can be applied to various plasma environments and justified that saturation can occur in general.

Based on the power balance equation, we found that as the plasma size increases, the effect of diffusion decreases, and the confinement increases. This causes an increase in electron density and a decrease in electron temperature. An enhancement of plasma confinement causes the increase of electron density by reducing diffusive loss. Conversely, the electron temperature decreases due to an increase in ionization.

Our global model simulations are simple yet provide valuable insights for cold plasmas. Our study serves as a guideline for controlling plasma parameters to control the generation of reactive species. The results presented in this study, in particular, the tendency of excited species according to the driving power, can be applied to various cold plasma sources.

Acknowledgements This work was partially supported by Samsung Electronics Co., Ltd (Grant No. IO201209-07922-01).

Data availability The data that support the fndings of this study are available from the corresponding author.

References

1. M. Ito et al., Plasma Process. Poly. **15**, 1700073 (2017)
2. M. Laroussi, IEEE Trans. Plasma Sci. **37**, 714 (2009)
3. K. Dieter et al., Pure Appl. Chem. **82**, 1223–1237 (2010)
4. T. Bernhardt et al., Oxid. Med. Cell. Longev. **2019**, 3873928 (2019)
5. J. Heinlin et al., J. Eur. Acad. Dermatol. Venereol. **25**, 1–11 (2011)
6. G. Daeschlein et al., IEEE Trans. Plasma Sci. **39**(2), 815–821 (2011)
7. Z. Xiong, J. Roe, T.C. Grammer, and D. B. Graves Plasma Process. Poly. **13**(6), 588–597 (2016)
8. A. Helmke et al., New J. Phys. **11**, 11 (2009)
9. G. Isbary et al., Br. J. Dermatol. **167**(2), 404–410 (2012)
10. G. Isbary et al., Br. J. Dermatol. **163**, 78–82 (2010)
11. A. Chuangsuwanich, T. Assadamongkol, D. Boonyawan, Int. J. Low. Extrem. Wounds **15**(4), 313–319 (2016)
12. J. Lee et al., IEEE Trans. Plasma Sci. **47**(11), 4833–4839 (2019)
13. C. Chutsirimongkol et al., Plasma Med. **4**(1–4), 79–88 (2014)
14. K.-H. Lee et al., Plasma Sci. Technol. **21**, 125403 (2019)
15. Y.-L. Men, P. Liu, X.-y Meng, Y.-X. Pan, Fire. Phys. Chem. **2**, 214–220 (2022)
16. C. Saka, Crit. Rev. Anal. Chem. **48**, 1–14 (2018)
17. Y.-l Men, P. Liu, X. Peng, Y.-X. Pan, Sci. China Chem. **63**, 1416–1427 (2020)
18. D. Jariwala et al., Chem. Soc. Rev. **42**, 2824–2860 (2013)
19. I.A. Kinloch, Science **362**, 547–553 (2018)
20. F. Liu et al., J. Phys. Chem. C **118**, 22760–22767 (2014)
21. E.P. Stuckert, E.R. Fisher Sensor, Actuat. B: Chem. **208**, 379–388 (2015)
22. L. Xu et al., J. Energy Chem. **35**, 24–29 (2019)
23. S. Jin et al., Inter. J. Hydrog. Energy **45**, 424–432 (2020)
24. Q. Li et al., J. Alloys Comp. **816**, 152610 (2020)
25. J. Zheng, X. Peng, Z. Wang, Phys. Chem. Chem. Phys. **23**, 6591–6599 (2021)
26. COMSOL, Inc. 2020 COMSOL Multiphysics Reference Manual (version 5.5). Available at www.comsol.com (accessed on September 10, 2020)
27. S.Y. Jeong, W.J. Nam, J.K. Lee, G.S. Yun, J. Phys. D: Appl. Phys. **51**, 454001 (2018)
28. M.A. Lieberman, A.J. Lichtenberg, *Principles of plasma discharges and materials processing*, 2nd edn. (Wiley, New York, 2005)
29. E.G. Thorsteinsson, J.T. Gudmundsson, Plasma Sources Sci. Technol. **19**, 015001 (2010)
30. Biagi-v7.1 database, private communication, www.lxcat.net, retrieved on November 8, 2021
31. S. Yueh-Jaw, M.A. Biondi, Phys. Rev. A **17**, 868 (1978)
32. Quantemol-DB. Avalaible at https://quantemoldb.com/ (accessed on November10, 2019)
33. A. Bultel, B. Van Ootegem, A. Bourdon, P. Vervisch, Phys. Rev. E **65**, 046406 (2002)
34. D.C. Lorents, Physica **82C**, 19–26 (1976)
35. F. Kannari, A. Suda, M. Obara, T. Fujioka, IEEE J. Quantum Electron. **19**, 1587–1600 (1983)
36. J. Vlcek, J. Phys. D **22**, 623 (1989)
37. S.K. Lam, C.-E. Zheng, D. Lo, A. Demyanov, A.P. Napartovich, J. Phys. D **33**, 242 (2000)
38. M.N. Rolin, S.I. Shabunya, J.C. Rostaing, J.M. Perrin, Plasma Sources Sci. Technol. **16**, 480 (2007)
39. N. Kang, F. Gaboriau, O. Soo-ghee, A. Ricard, Plasma Sources Sci. Technol. **20**, 035002 (2011)
40. George M. Petrov, Carlos M (2013) Ferreira arXiv:1308.2593
41. A. Bogaerts, R. Gijbels, J. Vlcek, J. Appl. Phys. **84**, 121–136 (1998)
42. R. Rincón, J. Munoz, M. Sáez, M.D. Calzada, Spectrochim. Acta B **81**, 26–35 (2013)